Contribution of Lattice Distortion to Solid Solution Strengthening in a Series of Refractory High Entropy Alloys

H. Chen[a]*, A. Kauffmann[a], S. Laube[a], I.-C. Choi[b], R. Schwaiger[b], Y. Huang[a], K. Lichtenberg[a], F. Müller[c], B. Gorr[c], H.-J. Christ[c], and M. Heilmaier[a]

[a] Institute for Applied Materials (IAM-WK), Karlsruhe Institute of Technology (KIT), Engelbert-Arnold-Str. 4, D-76131 Karlsruhe, Germany

[b] Institute for Applied Materials (IAM-WBM), Karlsruhe Institute of Technology (KIT), Hermann-von-Helmholtz-Platz 1, D-76344 Eggenstein-Leopoldshafen, Germany

[c] Institut für Werkstofftechnik, Universität Siegen, Paul-Bonatz-Str. 9-11, D-57068 Siegen, Germany

*corresponding author
mail: hans.chen@kit.edu, phone: +4972160846462

Abstract

We present an experimental approach for revealing the impact of lattice distortion on solid solution strengthening in a series of body-centered (bcc) Al-containing, refractory high entropy alloys from the Nb-Mo-Cr-Ti-Al system. By systematically varying the Nb and Cr content, a wide range of atomic size difference as a common measure for the lattice distortion was obtained. Single phase, bcc solid solutions were achieved by arc-melting and homogenization as well as verified by means of scanning electron microscopy (SEM) and X-ray diffraction (XRD). The atomic radii of the alloying elements for determination of atomic size difference were re-calculated on the basis of the mean atomic radii in and the chemical compositions of the solid solutions. Microhardness at room temperature correlates well with the deduced atomic size difference. Nevertheless, the mechanisms of microscopic slip lead to pronounced temperature dependence of mechanical strength. In order to account for this particular feature, we present a combined approach, using microhardness, nanoindentation and compression tests. The athermal proportion to the yield stress of the investigated equimolar alloys is revealed. These parameters support the universality of this aforementioned correlation. Hence, the pertinence of lattice distortion for solid solution strengthening in bcc high entropy alloys is proven.

1. Introduction

Since the introduction of high entropy alloys (HEAs) [1], the focus has especially been on their microstructural and mechanical properties [2]. Solid solution strengthening in such chemically complex alloys is of particular interest [3], as these systems typically exceed the constitutional range spanned by classical theories for the description of solid solution strengthening in dilute [4,5] and more concentrated [6] binary alloys. Accordingly, some efforts were made to develop models succeeding the current state of the description of solid solution strengthening [7–10]. The approach presented by Toda-Caraballo and Rivera-Díaz-del-Castillo [8] is based on the theory by Labusch [6] while it uses a generalization of the gradual changes of the lattice parameter and thus the misfit with composition in binary solid solution towards multi-component systems. In contrast, Varvenne, Luque and Curtin [10] presented a mechanistic, parameter-free and predictive theory for the yield strength of random alloys and face-centered cubic (fcc) HEAs, respectively, which was validated against data available for the CoCrFeMnNi system mainly contributed by Wu et al. [11]. The fundamental assumption is that dislocations move through an effective medium having average lattice parameter, shear modulus, stacking fault energy, etc. [10]. Strengthening accordingly arises from the interaction of dislocations with random, local concentration fluctuations around the average composition of the HEA [10]. This especially accounts for the fact that in case of HEAs solute and solvent cannot be distinguished due to their equal concentration. In conclusion of Ref. [10], alloys with maximized strength can be obtained by maximizing the concentration-weighted, mean-square misfit volume and/or the shear modulus. Assuming the validity of Vegard's law and using reasonable values for

51 individual atomic radii, the concentration-weighted, mean-square misfit volume which is used in this

52 theory can directly be transformed into the more common atomic size difference δ [10].

$$\delta = \sqrt{\sum_i x_i \left(1 - \frac{r_i}{\bar{r}}\right)^2} \tag{1}$$

53 where x_i is the molar fraction of the alloying element, r_i is the atomic radius of the respective alloying

54 element and $\bar{r}$ is the average atomic radius of the alloy. An extension of this procedure was introduced

55 by Okamoto et al. [9] by taking the individual mean-square atomic displacements of the alloying

56 elements into account. They propose a linear relationship of the yield strength and the averaged mean

57 square atomic displacement.

58 Strictly, the proposed theory by Varvenne, Luque and Curtin [10] does only apply to dislocation slip

59 with low impact of Peierls stress as it is observed for fcc metals and alloys. Nevertheless, lattice

60 distortion might significantly attribute to solid solution strengthening in bcc HEAs as well, and the

61 simplicity and elegance of the atomic size difference approach makes it worth to be tested for

62 correlation of δ with the plastic yield of bcc HEAs. In this case, the contribution to solid solution

63 strengthening might not be driven by the interaction of the elastic distortion field of dislocations and

64 the one of solute atoms but by the interaction of dislocation cores with random, local concentration

65 fluctuations as it is suggested by Rao et al. in Ref. [12]. Deviations from significant correlation might

66 lead to the identification of (i) interesting model alloys with non-equimolar composition and/or (ii)

67 additional contributions by short range ordering [13] as well as variations of local dislocation core

68 structures [12] specific to certain alloys.

69 Recently, we presented a suitable processing route for obtaining an almost single phase, bcc HEA

70 NbMoCrTiAl [14]. The basic design goal was to combine elements with high melting points (Nb, Mo)

71 and, thus, high intrinsic creep strength with protective oxide scale forming elements (Cr, Al) while

72 simultaneously reducing density (Al, Ti) by a proper choice of elements. Arc-melting and

73 homogenization treatment at 1300 °C for 20 h lead to an almost single phase microstructure that

74 possesses significant plasticity above 600 °C. Moreover, the formation of combined ⟨111⟩-/⟨001⟩-

75 fiber texture components with respect to the loading axis developing during compression testing at

76 these temperatures reveal dislocation slip with ⟨111⟩ Burgers vectors as it is expected for bcc

77 materials. The alloy exhibits a reasonable high temperature strength. Furthermore, the capability of

78 increasing oxidation resistance by adding Cr and Al has been verified for the present and related alloys

79 [15–18].

80 In general, large differences in atomic size which are expected for NbMoCrTiAl as well as its ability

81 to deform by dislocation slip makes it a favorable model system for studying the impact of the

82 contribution of lattice distortion to solid solution strengthening in bcc HEAs. For this purpose, suitable

83 changes in alloy composition and the according homogenization treatment for obtaining single phase

84 microstructure were established and are presented in this article. In order to quantitatively describe the
85 lattice distortion in the present alloys, lattice parameters and, thus, interatomic spacings were
86 determined by means of XRD. These data are used to re-calculate the individual atomic radii of the
87 alloying elements with the coordination of a bcc lattice. Finally, the according atomic size difference is
88 correlated with mechanical properties exhibited by the alloy series. In order to account for the
89 temperature-dependent strength of bcc metals, a suitable combination of microhardness for screening
90 at room temperature as well as nanoindentation up to 400 °C and compression tests for temperatures
91 beyond 400 °C were exemplarily conducted. The relevance of the microhardness results at room
92 temperature of the respective alloys is stressed.

2. Experimental

94 The alloys investigated in this work were manufactured from elemental bulk material. Nb, Mo, Cr, Ti
95 and Al with a purity of 99.9 %, 99.96 %, 99 %, 99.8 %, and 99.9 %, respectively, were mixed in the
96 desired concentrations and then melted under Ar atmosphere, using an AM/0.5 arc melting furnace by
97 Edmund Bühler GmbH (Germany). The furnace chamber was set to a pressure of $5 \cdot 10^{-2}$ mbar and
98 alternatingly evacuated and flooded with Ar for three times, before pumping to a high vacuum of less
99 than $1 \cdot 10^{-4}$ mbar. The Ar pressure for arc melting was set to 600 mbar. A Zr getter was liquefied
100 prior to each melting step to reduce residual oxygen content. The melted buttons were flipped and re-
101 melted for at least five times and optionally cast into a water-cooled rod-shaped Cu mold with a
102 diameter of 12 mm and length of 60 mm. Compositions of the equiatomic alloys in as-cast state were
103 determined by inductively coupled plasma optical emission spectrometry (ICP-OES). O and N content
104 were analyzed by means of carrier gas hot extraction analysis by a TC500 device (Leco Instrumente
105 GmbH). Depending on the alloy composition, homogenization was performed under Ar atmosphere in
106 a Gero HTRH 70-600/18 resistance tube furnace for 20 h at 1200, 1300, 1400 and 1500 °C. For this
107 purpose, buttons and rods were cut into platelets with a thickness of 5 mm. The heating and cooling
108 rates were 4.2 K/min. Subsequent to face-grinding, XRD analyses (step width for acquisition 0.01°,
109 acquisition time of 384 s/step) were carried out on a D2 Phaser system by Bruker equipped with a
110 Lynxeye line detector. The lattice parameter was determined by extrapolating towards $\Theta = 90°$ using
111 the following weighting function $\frac{1}{2}(\cot^2\Theta + \cot\Theta \cdot \cos\Theta)$ according to Nelson-Riley [19]. For
112 microstructural investigations, the samples were prepared by a standard metallographic procedure.
113 After grinding with a series of abrasive papers of decreasing grain size, the samples were polished,
114 etched with NH_3, H_2O_2 and distilled water in a ratio of 1:1:1 at 50 °C for 5 min and finalized by a
115 vibratory polishing step for 8 h, using a non-crystallizing oxide polishing suspension with pH = 9.8
116 supplied by Struers. SEM and energy dispersive X-ray spectroscopy (EDX) analysis were performed
117 on a Zeiss EVO50 system equipped with a Thermo Scientific EDX system. For each equiatomic alloy,

porosity was investigated in terms of area fraction which was determined from several binarized SEM micrographs. The investigated area was 1.2 mm^2, respectively.

Mechanical properties were characterized in terms of yield stress and hardness. Yield stress σ_y during compression tests was determined for 0.2 % plastic strain at elevated temperatures in a range of 400 °C up to 1200 °C at an initial engineering strain rate of 10^{-3} s^{-1}. The samples of (3 x 3 x 4.5) mm^3 were tested under vacuum in a Zwick Z100 electromechanical universal testing machine equipped with a vacuum furnace by Maytec. Strain was determined using strain gauges attached to the samples. Vickers hardness μH was investigated by a Qness Q10A+ microhardness tester with a load of 0.98 N. Mean values and standard deviations were obtained by analyzing 16 hardness indentations on each sample. Furthermore, a nanoindenter G200XP by Keysight Technologies GmbH equipped with a laser heating stage by SURFACE systems + technology GmbH was utilized to measure temperature-dependent nanohardness nH between room temperature and 400 °C at a constant indentation strain rate of $5 \cdot 10^{-2}$ s^{-1}. Strain-rate sensitivity $m = (\frac{\partial \ln \sigma_y}{\partial \ln \dot{\varepsilon}})_{\varepsilon,T} = (\frac{\partial \ln(\frac{nH}{C})}{\partial \ln \dot{\varepsilon}})_{\varepsilon,T}$ [20,21] (σ_y: yield stress, $\dot{\varepsilon}$: strain rate, T: temperature, nH: nanohardness, C: constraint factor, usually $C \approx 3$ [22]) was analyzed from room temperature up to 300 °C by strain-rate jump tests with strain rates of $5 \cdot 10^{-2}$ s^{-1}, $1.6 \cdot 10^{-2}$ s^{-1} and $5 \cdot 10^{-3}$ s^{-1}. Shear modulus G of selected alloys was calculated by $G = \frac{1}{1-p} \cdot \rho \cdot v_T^2$ (p: porosity; ρ: density; v_T: velocity of transverse ultrasonic waves). The experimentally determined density ρ comprises an error that arises from the sample porosity p and is corrected by the factor $\frac{1}{1-p}$ of the aforementioned equation. The density was determined by Archimedes principle, v_T was analyzed by ultrasonic phase spectroscopy on cubic samples with an edge length of 5 mm within the frequency range of 5 kHz to 10 MHz using two identical broadband ultrasonic wave transducers (Panametrics model V155) and a R3754A network analyzer by Advantest. Ref. [23] provides further experimental details of ultrasonic phase spectroscopy.

3. Results and discussion

Microstructure

Prerequisite for the accurate assessment of solid solution strengthening is a homogenous microstructure of the alloys under investigation. In the following, this is exemplified with the three equimolar compositions which were manufactured for this work. All non-equiatomic compositions were treated in similar ways in order to ensure homogeneity of the solid solution. Starting point for the development was the aforementioned homogeneous, quinary, equimolar NbMoCrTiAl alloy which can be manufactured by arc-melting and subsequent homogenization treatment [14]. After heat-treatment of the as-cast state at 1300 °C for 20 h, an almost single phase microstructure as presented in Fig. 1b
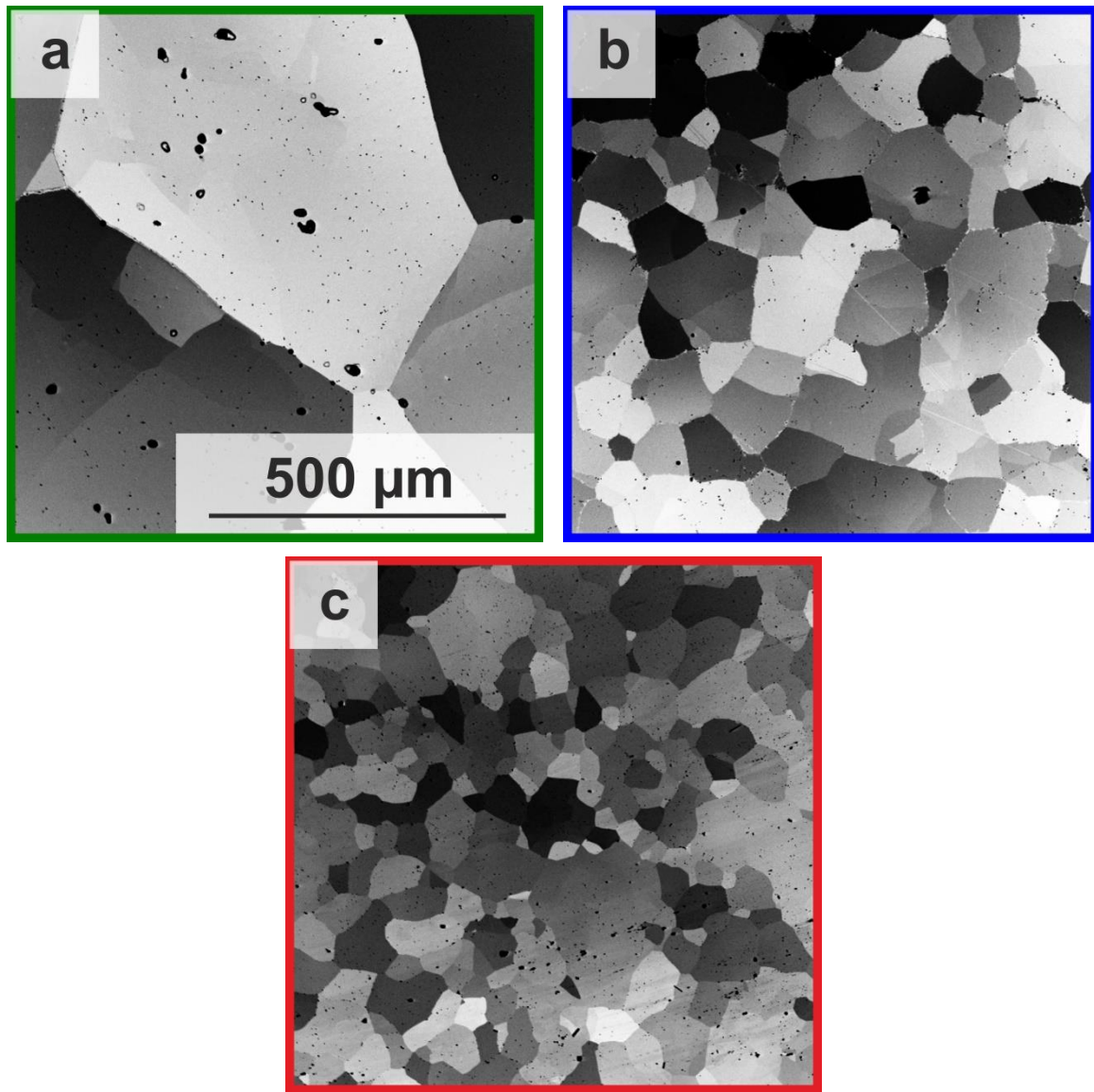
150 can be obtained for this alloy. The XRD pattern in Fig. 2b reveals the bcc crystal structure (W

151 prototype, Strukturbericht A2).

152 During development of this alloy, several phases competing with the bcc solid solution were identified.

153 Most importantly, the formation of the hexagonal Cr_2Nb-Laves phase ($MgZn_2$ prototype,

154 Strukturbericht C14) has to be suppressed for retaining single phase bcc. In NbMoCrTiAl, the Laves

155 phase appears for homogenization heat-treatments below 1300 °C as well as during compression

156 testing of as-homogenized material at 1200 °C. Moreover, $(Mo,Nb)_3Al$ (Cr_3Si prototype,

157 Strukturbericht A15) forms during annealing at all temperatures tested for homogenization up to now[1].

158 Nevertheless, this phase appears only as a fringe of tiny dimension in the vicinity of some grain

159 boundaries. For 1300 °C and 20 h, its volume fraction is below 0.3 vol% in total and can thus be

160 considered to be not a relevant factor for the mechanical properties determined in this work. Some

161 trace contents of $(Al,Cr)_3Ti$ (Cu_3Au prototype, Strukturbericht D0$_9$) as well as B2 superstructure can

162 occasionally be found for a variety of processing conditions but are as well believed to be not relevant

163 for mechanical property determination. All aforementioned phases were identified based on global

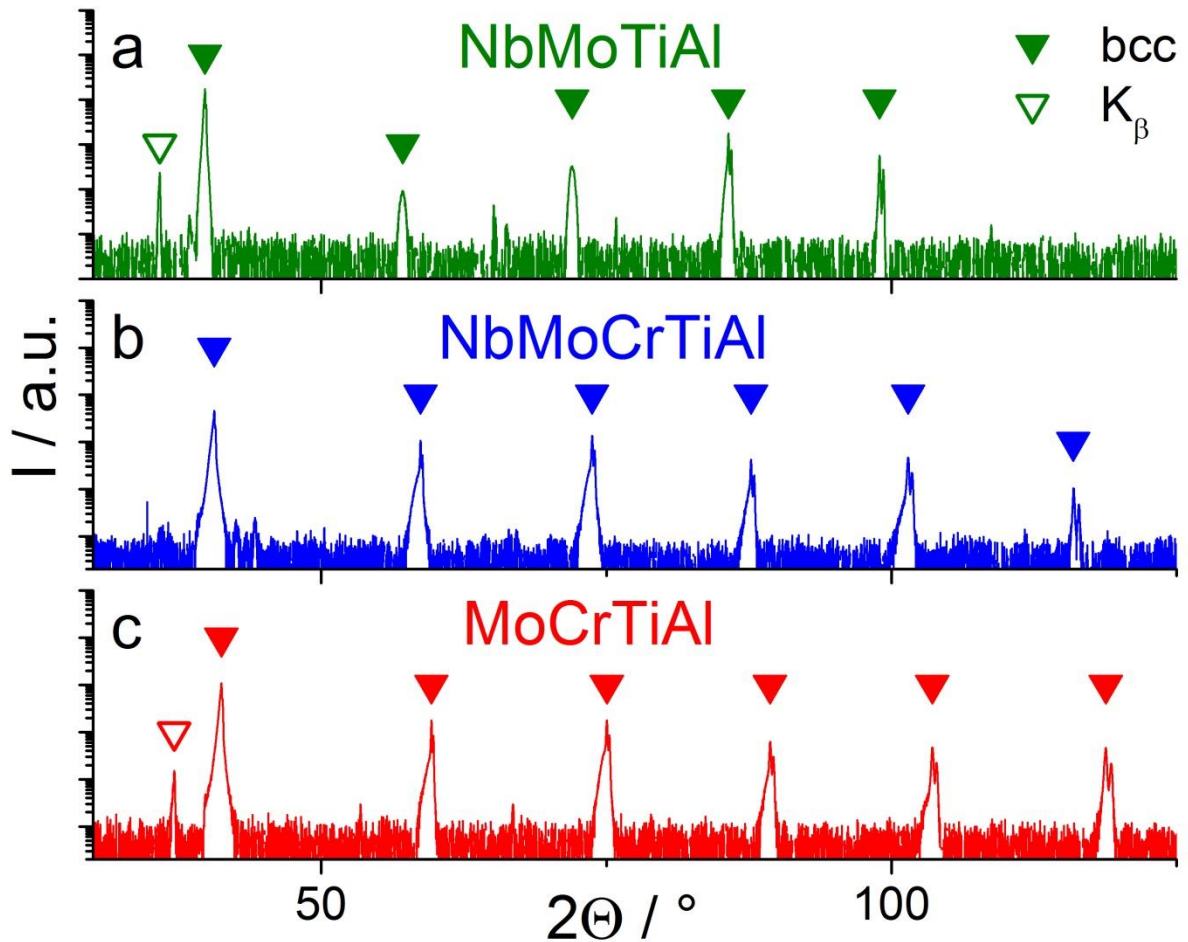164 XRD patterns as well as locally by means of EBSD patterns.

165 Since most of the competing phases are expected for varying alloy compositions derived from

166 NbMoCrTiAl, only specific changes of alloying elements were conducted in this research. For the

167 suppression of Laves phase formation, either Nb or Cr content was successively reduced towards the

168 quaternary, equimolar alloys NbMoTiAl and MoCrTiAl. In case of NbMoTiAl, a significantly higher

169 homogenization temperature was needed in order to achieve a homogeneous bcc solid solution,

170 namely 1500 °C for 20 h. The according microstructure and the XRD pattern are presented in Figs. 1a

171 and 2a, respectively. In contrast, annealing at only 1200 °C for 20 h is necessary to obtain single phase,

172 bcc MoCrTiAl shown in Figs. 1c and 2c. The concentrations of Mo, Ti and Al were kept constant. It

173 was expected that increasing Mo, Ti and Al in Nb-Mo-Cr-Ti-Al could favor the formation of

174 $(Mo,Nb)_3Al$ and $(Al,Cr)_3Ti$ while reducing the amount of these particular elements could lead to

175 stabilization of Cr_2Nb.

---

[1] This phase remained unidentified in our previous investigation [14].

Figure 1: Microstructure of alloys with equiatomic composition in homogenized condition, obtained by SEM using BSE contrast imaging (same magnification for all images): (a) NbMoTiAl annealed at 1500 °C, (b) NbMoCrTiAl annealed at 1300 °C and (c) MoCrTiAl annealed at 1200 °C, each for 20 h. Certain porosity (black features within the grains) is typical for cast material (< 2 vol.% in all presented alloys) and was randomly distributed in both as-cast (not presented in this article) and as-homogenized state.

Figure 2: XRD patterns with logarithmic intensity scale of alloys with equiatomic composition in homogenized condition: (a) NbMoTiAl annealed at 1500 °C, (b) NbMoCrTiAl annealed at 1300 °C and (c) MoCrTiAl annealed at 1200 °C, each for 20 h. Peaks arising from residual Cu-Kβ radiation are indicated by open triangles $\triangledown$.

Tab. 1 summarizes all investigated alloys, their compositions and the necessary heat-treatments to obtain almost single phase microstructures with residual phases having a total volume fraction of less than 0.5 vol%. In certain cases, higher homogenization temperatures were used as well in order to exclude effects by the grain size of the material and possible influences by the homogenization temperature (e. g. different extent of any type of ordering) on the mechanical response. For NbMoCrTiAl, several batches were tested for assessment of the reproducibility.

Table 1: Composition in at.% of solid solutions in annealed condition determined by standard-related EDX as well as lattice parameters of the bcc structure; O contents were exemplarily analyzed for NbMoTiAl, NbMoCrTiAl and MoCrTiAl: 780 at.ppm, 312 at.ppm and 289 at.ppm, respectively. N content was below the detection limit for all tested alloys. ♦ highlights EDX on a different batch [14], * were used for re-calculation of the atomic radii.

j	nominal	annealing		$x_{i,j}$		a_j^{bcc} / nm

|	composition	condition	Nb	Mo	Cr	Ti	Al	
	NbMoTiAl	1400 °C, 20 h	0.251 ± 0.001	0.248 ± 0.002	-	0.253 ± 0.002	0.248 ± 0.001	
1		1500 °C, 20 h*	0.252 ± 0.001	0.249 ± 0.001	-	0.252 ± 0.001	0.247 ± 0.001	$3.208^{+0.018}_{-0.007}$
2	NbMoCr$_{0.25}$TiAl	1300 °C, 20 h*	0.259 ± 0.00.1	0.233 ± 0.00.1	0.058 ± 0.001	0.230 ± 0.001	0.220 ± 0.000	$3.198^{+0.002}_{-0.058}$
3	NbMoCr$_{0.5}$TiAl	1300 °C, 20 h*	0.234 ± 0.001	0.226 ± 0.003	0.099 ± 0.001	0.216 ± 0.001	0.225 ± 0.001	$3.175^{+0.018}_{-0.013}$
		1400 °C, 20 h	0.231 ± 0.000	0.223 ± 0.001	0.101 ± 0.001	0.216 ± 0.000	0.228 ± 0.000	
4	NbMoCr$_{0.75}$TiAl	1300 °C, 20 h*	0.234 ± 0.001	0.208 ± 0.003	0.157 ± 0.003	0.204 ± 0.001	0.197 ± 0.001	$3.165^{+0.035}_{-0.005}$
5	NbMoCrTiAl	1300 °C, 20 h*	0.219 ± 0.001	0.201 ± 0.002	0.200 ± 0.002	0.192 ± 0.000	0.187 ± 0.001	$3.149^{+0.021}_{-0.004}$
		1400 °C, 20 h	0.219 ± 0.001	0.197 ± 0.001	0.195 ± 0.001	0.191 ± 0.000	0.198 ± 0.000	
		1300 °C, 20 h♦	0.205 ± 0.001	0.195 ± 0.000	0.197 ± 0.001	0.205 ± 0.002	0.199 ± 0.001	
6	Nb$_{0.75}$MoCrTiAl	1300 °C, 20 h*	0.173 ± 0.001	0.214 ± 0.001	0.208 ± 0.000	0.205 ± 0.000	0.200 ± 0.001	$3.141^{+0.048}_{-0.011}$
7	Nb$_{0.5}$MoCrTiAl	1300 °C, 20 h*	0.112 ± 0.000	0.232 ± 0.002	0.221 ± 0.001	0.215 ± 0.001	0.220 ± 0.000	$3.127^{+0.044}_{-0.011}$
		1400 °C, 20 h	0.110 ± 0.000	0.228 ± 0.001	0.218 ± 0.001	0.218 ± 0.001	0.226 ± 0.002	
8	Nb$_{0.25}$MoCrTiAl	1300 °C, 20 h*	0.065 ± 0.001	0.241 ± 0.002	0.238 ± 0.002	0.234 ± 0.001	0.222 ± 0.001	$3.114^{+0.006}_{-0.009}$
9	MoCrTiAl	1200 °C, 20 h*	-	0.253 ± 0.001	0.248 ± 0.000	0.245 ± 0.001	0.254 ± 0.001	$3.101^{+0.018}_{-0.006}$
		1300 °C, 20 h	-	0.254 ± 0.002	0.247 ± 0.002	0.242 ± 0.000	0.257 ± 0.001	

197

Atomic radii of the alloying elements

In principle, three degrees of complication of the description of the variation of the lattice in a HEA are possible. The easiest assumption is that the HEA has a defined lattice parameter without a variation on atomic length scale at all. This assumption is physically not meaningful and would lead to the conclusion that there is no hardening since the solute atoms do not have a distortion field. Further complication is possible by assuming an effective lattice parameter of the alloy as well as its variation caused by the individual size of the alloying elements – this variation might be used as a measure for the lattice distortion. Even more complex is a description where each species of alloying elements has an average size and an according variation. In this case, the exact size of an atom is determined by the actual environment of the atom (not by its species alone as it is assumed in the previous case). Despite the latter case being the most realistic description and providing several quantities for the lattice distortion, the second assumption already allows for a possible description of solid solution strengthening. Furthermore, the second case is rather easy to be assessed when the atomic radii of the alloying elements within the solid solution are known. As pointed out by Varvenne, Luque and Curtin [10], the assessment of atomic size difference based on the (tabulated) atomic radii of the pure elements might lead to arbitrary results when the pure elements crystallize in a different crystal structure as compared to the HEA solid solution. In such case, the binding state of the alloying element is different and accordingly a different contribution to the lattice distortion has to be expected.

216   In the present work, we try to obtain reasonable atomic radii by analyzing all obtained bcc alloys

217   (coordination number CN = 8). In the case of the crystal structure being constant, binding state

218   remains rather constant. Furthermore, only the refractory elements Nb and Cr are changed in their

219   concentrations which should further reduce the possibility of varying amounts of directed binding. The

220   situation might be different when Al or Ti content is changed over a wide composition range. For the

221   analyses of the data, an over-determined set of equations is formulated on the basis of: (i) the chemical

222   compositions $x_{i,j}$ presented in Tab. 1, where i is the respective alloying element and j the respective

223   alloy; (ii) the mean atomic radius $\bar{r}_j$ in the alloys obtained from $\bar{r}_j = \sqrt{3}/4 \cdot a_j^{\text{bcc}}$ (CN = 8) where a_j^{bcc}

224   are the lattice parameters presented in Tab. 1 which were determined by XRD. Moreover, the atomic

225   radii of the bcc crystallizing elements are included in the calculation as well (CN = 8). The

226   overdetermined set of equations reads thus

$$
\begin{pmatrix}
1 & 0 & 0 & 0 & 0 \\
0 & 1 & 0 & 0 & 0 \\
0 & 0 & 1 & 0 & 0 \\
x_{\text{Nb},1} & x_{\text{Mo},1} & x_{\text{Cr},1} & x_{\text{Ti},1} & x_{\text{Al},1} \\
x_{\text{Nb},2} & x_{\text{Mo},2} & x_{\text{Cr},2} & x_{\text{Ti},2} & x_{\text{Al},2} \\
x_{\text{Nb},3} & x_{\text{Mo},3} & x_{\text{Cr},3} & x_{\text{Ti},3} & x_{\text{Al},3} \\
& & \vdots & &
\end{pmatrix}
\cdot
\begin{pmatrix}
r_{\text{Nb}} \\
r_{\text{Mo}} \\
r_{\text{Cr}} \\
r_{\text{Ti}} \\
r_{\text{Al}}
\end{pmatrix}
=
\begin{pmatrix}
r_{\text{Nb}} \\
r_{\text{Mo}} \\
r_{\text{Cr}} \\
\bar{r}_1 \\
\bar{r}_2 \\
\bar{r}_3 \\
\vdots
\end{pmatrix}
\tag{2}
$$

227

228   and is solved with respect to r_{Nb}, r_{Mo}, r_{Cr}, r_{Ti} and r_{Al} by a least-square procedure. The over-determined

229   set of equations is in principle a multi-component extension of Vegard's law. Fig. 3 shows the

230   comparison of the atomic radii of the elements (CN = 12 for Al and Ti; CN = 8 for Mo, Cr and Nb as

231   well as for an extrapolation for Ti designated as Ti*), the mean radii in the alloys deduced from the

232   bcc lattice parameter (CN = 8) as well as the values obtained from solving the aforementioned over-

233   determined set of equations. Since Ti exhibits a bcc high temperature modification, a second atomic

234   radius for Ti based on the lattice parameter of the high temperature bcc phase (CN = 8) and

235   compensated by thermal expansion down to room temperature taken from Ref. [24] is included as a

236   reference as well. It is obvious, that the atomic radii of all elements which are deduced from non-bcc

237   crystal structures, namely Al and Ti, are quite different from the re-calculated atomic radii whereas the

238   radii of the bcc elements are well reflected by this approach. A good agreement of the re-calculated

239   atomic radii with the experimentally observed mean atomic radii in the alloys of the present

240   contribution is found. It is pointed out that the error indication for the experimental mean atomic radii

241   is conservatively chosen (taking the peak width into account) in all cases and might be significantly

242   smaller in reality. Thus, the description of alloys within the Nb-Mo-Cr-Ti-Al system on the basis of

243    $r_{\text{Nb}} = 1.4297$ Å, $r_{\text{Mo}} = 1.3627$ Å, $r_{\text{Cr}} = 1.2488$ Å, $r_{\text{Ti}} = 1.4474$ Å and $r_{\text{Al}} = 1.3172$ Å is rather good

244   and the linearity by Vegard's law seems to be reasonable – at least for variations of the Cr and Nb

245   concentration. Further details of the binding states in such alloys have to be investigated in future –

246 especially with respect to individual variation of the radii of the elements which will not be considered

247 for the further course of this article. Also, the actual misfit volume was not experimentally determined

248 within this work, but would describe the extent of lattice distortion in an even more accurate way.
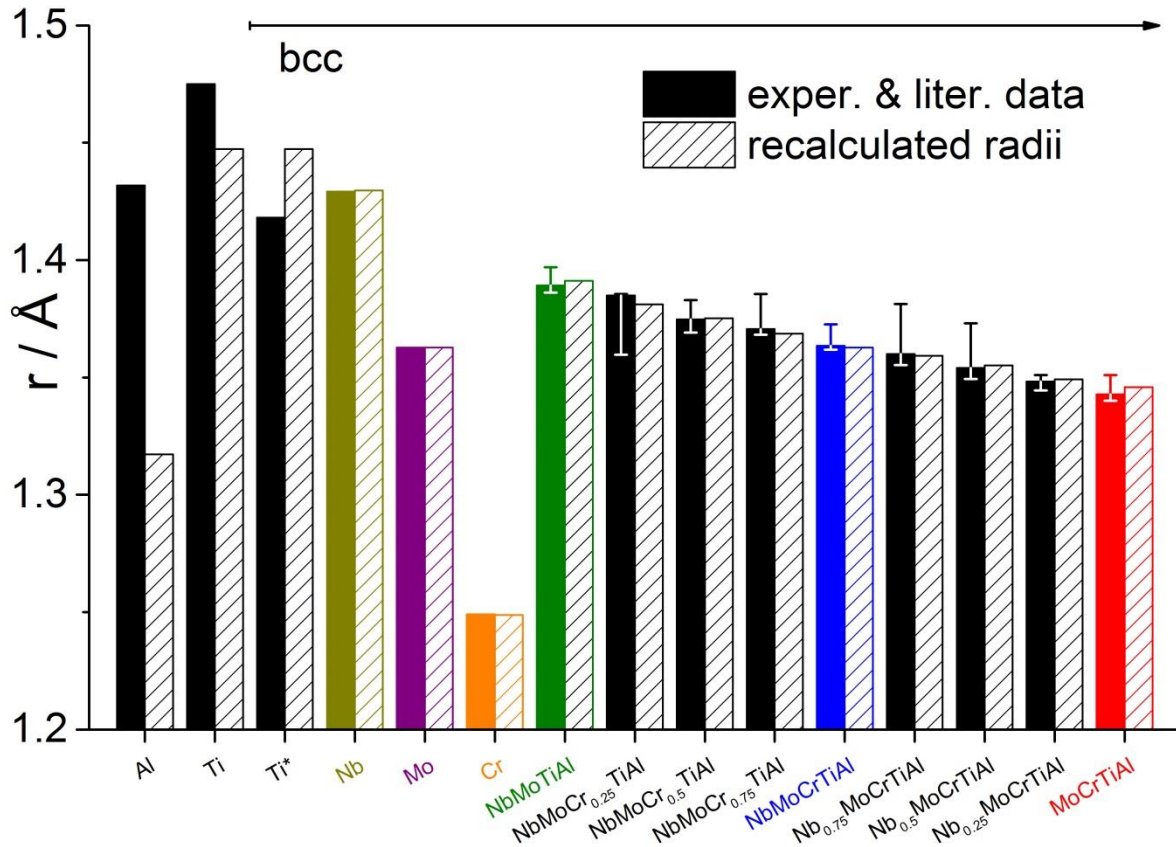
249 Figure 3: Comparison of experimental and re-calculated atomic radii in the elements r_i as well as

250 investigated alloys $\bar{r}_j$. Literature data for Al, Ti (using CN = 12, respectively), Nb, Mo and Cr (using

251 CN = 8), respectively, represented by solid bars are all taken from [25], "Ti*" designates an

252 extrapolation of the atomic radius of bcc Ti corrected by thermal expansion down to room temperature

253 (CN = 8) according to Ref. [24].

Temperature-dependent mechanical properties

255 Depending on the homologous temperature, bcc metals and substitutional solid solutions exhibit an

256 intrinsic temperature-dependent yield stress which can be divided into a low-temperature, a plateau

257 and a high-temperature regime, as exemplarily shown for Fe-3wt%Si in Refs. [26,27]. This is

258 schematically presented in Fig. 4a. At low temperatures, plastic deformation of bcc metals and alloys

259 is thought to be mediated by the thermally activated formation and movement of kink pairs. The

260 movement of kink pairs itself can be controlled by (i) either line-tension when the critical kink width

261 is very small and of the order of the dimension of the dislocation cores or the distance between minima

262 in the Peierls potential or (ii) by the elastic interaction of the kinks when the kink width is necessarily

high [28]. Consequently, strength increases considerably with (i) decreasing temperature and (ii) increasing strain rate. Above a certain temperature, usually referred to as "critical temperature" [29] or "knee-temperature" [21,28] a strength plateau is reached. In this temperature regime, strength becomes virtually strain-rate independent. The knee temperatures of the bcc principal elements of the present HEA system are about 130 °C for Nb, 275 °C for Mo and 300 °C for Cr [21,30]. For the investigated alloys a similar temperature range for the knee temperature is expected. When exceeding about $0.4 \cdot T_m$, (T_m: melting temperature) diffusional processes lead to rapid decrease of the yield stress. Mechanical strength becomes strain-rate dependent again. Thus, for the assessment of solid solution strengthening in bcc alloys the strain-rate independent plateau strength, frequently referred as athermal strength, should be ideally investigated.

In order to account for temperature dependence of the mechanical properties, several mechanical tests were performed and are summarized in Figs. 4b and c, respectively. Compression tests performed from 400 °C up to 1200 °C on the equiatomic alloys in Fig. 4c reveal the transition from plateau-like yield stress to creep-controlled strength. As shown in previous investigations, the predominant deformation mechanism in NbMoCrTiAl is dislocation slip up to a deformation temperature of 1200 °C [14]. Hence, this quinary alloy and its derivatives are well suited to discuss the temperature-dependent yield stress, also in the creep regime. Onset of the drop of strength is observed between 600 °C (MoCrTiAl) and 1000 °C (NbMoCrTiAl).

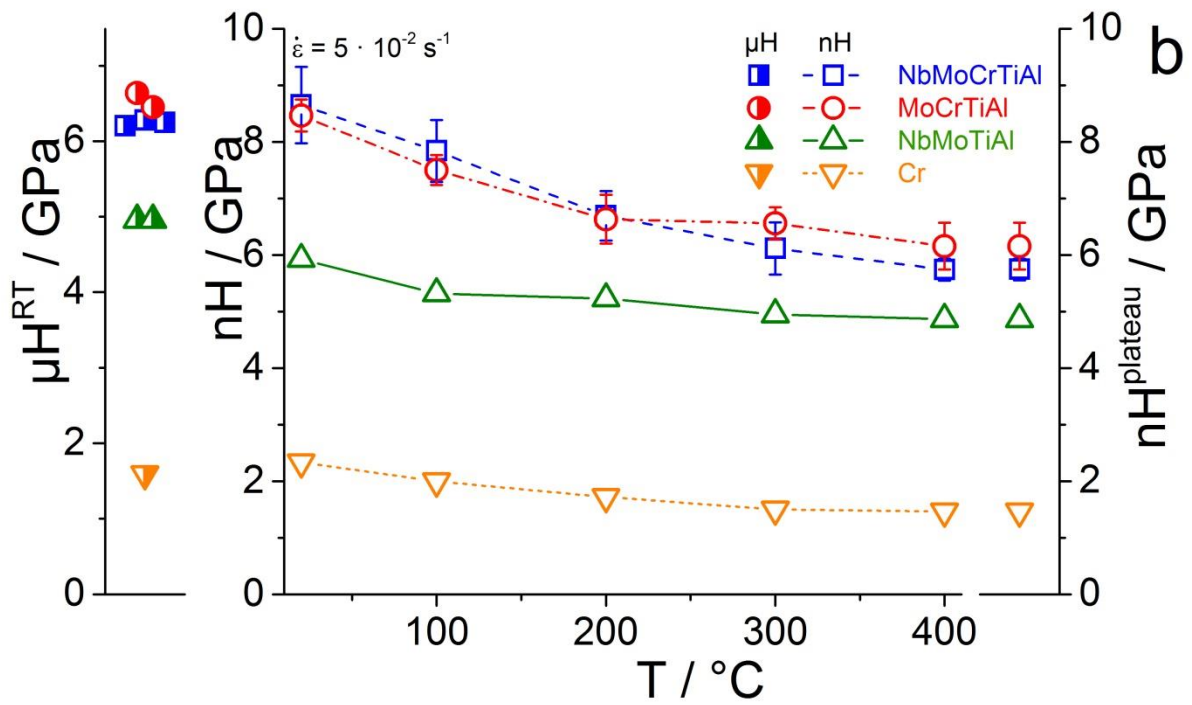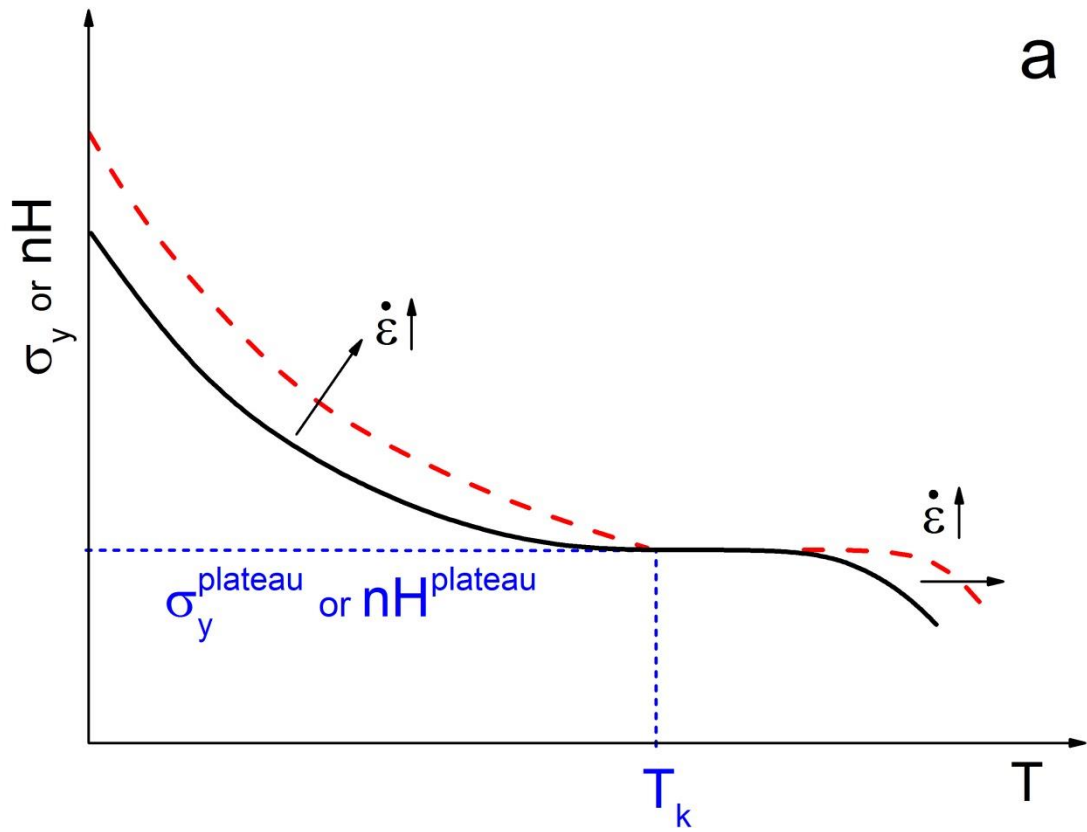Due to microstructural features, NbMoCrTiAl and its derivatives do not reveal significant plasticity on a macroscopic scale at temperatures lower than 600 °C (NbMoTiAl, NbMoCrTiAl) and 400 °C (MoCrTiAl). As shown in Fig. 1 and discussed in Ref. [14], abnormal grain growth appears during homogenization – this might lead to increasing compatibility stresses between these large grains and the surrounding microstructure during compression testing. This is a possible reason for a limited ductility of the presented alloys. In addition, pores within the compression samples, developed during solidification after casting, further lead to an increase of internal stresses due to localization. Thus, crack formation is initiated although, macroscopically, yield stress has not been reached. Nevertheless, microhardness and nanoindentation reveal plasticity (without cracking) on a local scale. Fig. 5 exemplarily shows slip traces of $NbMoCr_{0.5}TiAl$ in the vicinity of a microhardness indent at room temperature.
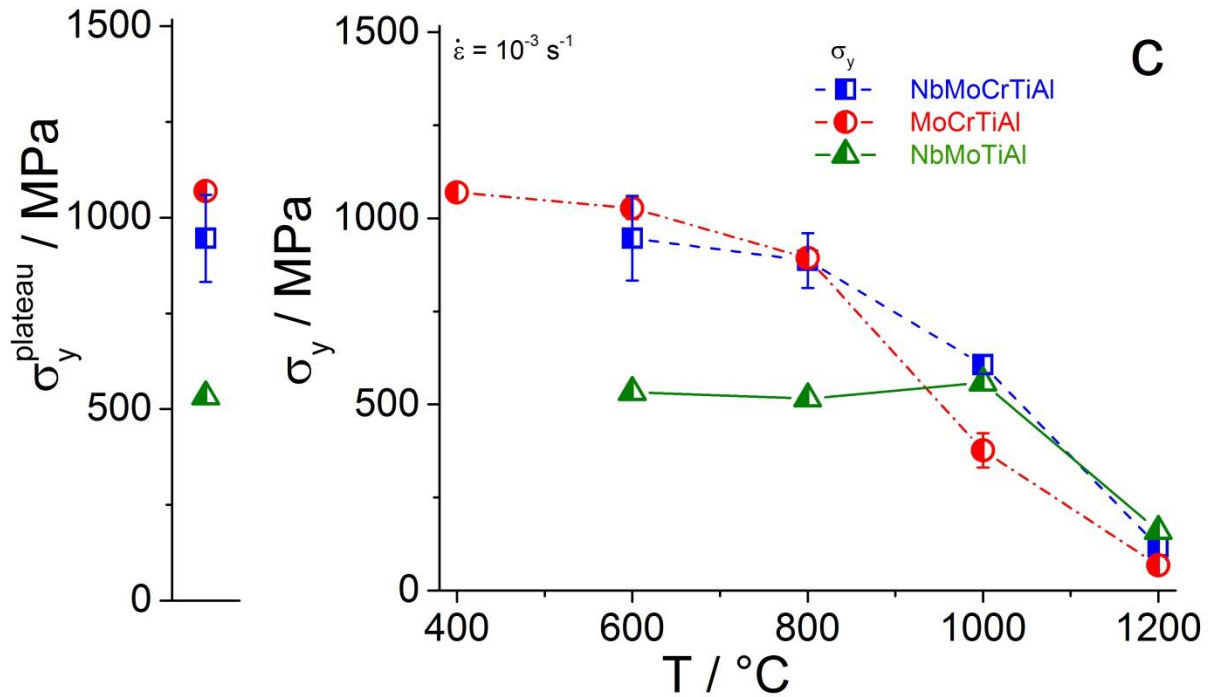
By using nanoindentation, a temperature range between RT and 400 °C could be covered in order to reveal the plateau region of the yield stress in Fig. 4b. Further details about the temperature-dependent nanohardness of pure Cr can be found elsewhere [21]. It has to be taken into account that indentation tests are typically affected by varying work hardening behavior due to higher plastic strains when compared to uniaxial tests for yield stress determination. Typically, hardness determined with a Berkovich indenter corresponds to a yield stress at about 7 % plastic strain [22]. Hence, contribution of work hardening to strengthening that occurs from indentation eventually varies with alloy

299   composition. Further alloy development with respect to ductility might provide chances to assess this

300   in the plateau temperature range. In agreement with the observations from compression testing, the

301   nanohardness data indicate a plateau of the mechanical strength at temperatures higher than

302   approximately 300 °C for the quaternary and quinary alloys. The temperature-dependent strain-rate

303   sensitivity was exemplarily investigated for NbMoCrTiAl in order to verify that the plateau hardness

304   is indeed achieved.

305   Compared to the rate-sensitive deformation behavior of pure bcc-structured elements in the low

306   temperature regime, such as Cr with a strain-rate sensitivity of about $m^{RT} = 0.08$ [21,29] at room

307   temperature, NbMoCrTiAl shows an already, comparably low $m^{RT} = 0.018 \pm 0.004$ at room

308   temperature. Nevertheless, as is in the case of pure Cr [21,29], the strain-rate sensitivity of

309   NbMoCrTiAl almost vanishes when approaching the knee temperature: $m^{300\,°C} = 0.007 \pm 0.003$.

310   Thus, clearly the plateau strength $\sigma_y^{plateau}$ is reached in the temperature range between 300 °C and

311   600 °C in NbMoCrTiAl. This is in agreement with our observations by compression tests at elevated

312   temperatures. In accordance, the chosen values for $nH^{plateau}$ and $\sigma_y^{plateau}$ are included as separate

313   charts in Figs. 4b and c, respectively.

314   The assessment of solid solution strengthening in the last part of the present article will be mainly

315   based on microhardness measurements at room temperature μH^{RT} due to their simplicity and

316   reproducibility. μH^{RT} does not significantly depend on alloy batch or varying homogenization

317   parameters. Hence, it is independent of grain size, grain orientation and RT hardness is reproducible.

318   As shown in Fig. 4b, strength and hardness at room temperature are already influenced by the

319   thermally activated slip processes. Nevertheless, microhardness μH^{RT} at room temperature on the one

320   hand and $nH^{plateau}$ as well as $\sigma_y^{plateau}$ on the other hand exhibit a very reasonable correlation (please

321   compare Figs. 4b and c).

a

b

Figure 4: a) Scheme of the temperature-dependent yield stress of bcc metals and alloys. Experimental results for the temperature dependence of the equiatomic alloys MoCrTiAl, NbMoTiAl and NbMoCrTiAl: b) Microhardness μH^{RT} was obtained at room temperature. Multiple data points represent μH^{RT} obtained for varying homogenization parameters and on different batches (please see Tab. 1). Nanohardness nH was determined between room temperature and 400 °C in order to obtain the plateau nanohardness $nH^{plateau} = nH(400°C)$. c) Compression tests were performed at a consistent strain rate of $10^{-3}s^{-1}$ between 400 °C and 1200 °C depending on the macroscopic ductility of the polycrystalline material in order to obtain the plateau yield stress $\sigma_y^{plateau}$ equal to $\sigma_y^{600°C}$ (NbMoCrTiAl, NbMoTiAl) and $\sigma_y^{400°C}$ (MoCrTiAl). The connecting lines are guiding the eyes. Error bars that do not exceed the symbol size are omitted.

Figure 5: Secondary electron (SE) contrast image of a Vickers indent (lower right corner) in NbMoCr$_{0.5}$TiAl at room temperature, revealing slip traces in various directions in the vicinity of the indent; slip traces are highlighted by black arrows.

Assessment of solid solution strengthening

By using the atomic radii presented in Fig. 3, the atomic size difference δ was calculated. While the mean atomic radius, calculated from the lattice parameters presented in Tab. 1, is monotonically decreasing with increasing Cr content from NbMoTiAl to NbMoCrTiAl and further decreases by decreasing the Nb content from NbMoCrTiAl to MoCrTiAl, atomic size difference exhibits a different trend. Fig. 6a shows that for alloys between NbMoTiAl and NbMoCrTiAl, monotonic increase of δ is observed, while it is almost constant for alloys between NbMoCrTiAl and MoCrTiAl. This is caused by the significant difference of the size of Cr compared to the average atomic size of the alloy while Nb exhibits a size similar to mean atomic radii of the prepared alloys and, thus, provides negligible potential for additional lattice distortion. Nevertheless, all presented alloys based on Nb-Mo-Cr-Ti-Al exhibit a δ ranging from 3.25 to 5.15 %. Thus, a significant variation of lattice distortion for investigating solid solution strengthening is provided. For reference, Cr, Mo and Nb without any lattice distortion are investigated, too.

For the assessment of the effect of δ on the mechanical properties, microhardness at room temperature μH^{RT} and plateau yield stress $\sigma_y^{plateau}$ are plotted in a unified way in Fig. 6a. Varying homogenization treatments as well as varying alloy batches (different data points in Fig. 6a, see Tab. 1 for details) do not significantly alter microhardness of the alloys. For reference, μH^{RT} of Nb, Cr and Mo are presented as well. Indeed, atomic size difference and microhardness seem to correlate. In the case of the alloy series ranging from NbMoCrTiAl to MoCrTiAl where constant mechanical strength should be expected, an excess hardness of about 0.8 to 0.9 GPa above the average microhardness of NbMoCrTiAl to MoCrTiAl of 6.3 GPa is observed. Staying approximately constant from NbMoTiAl
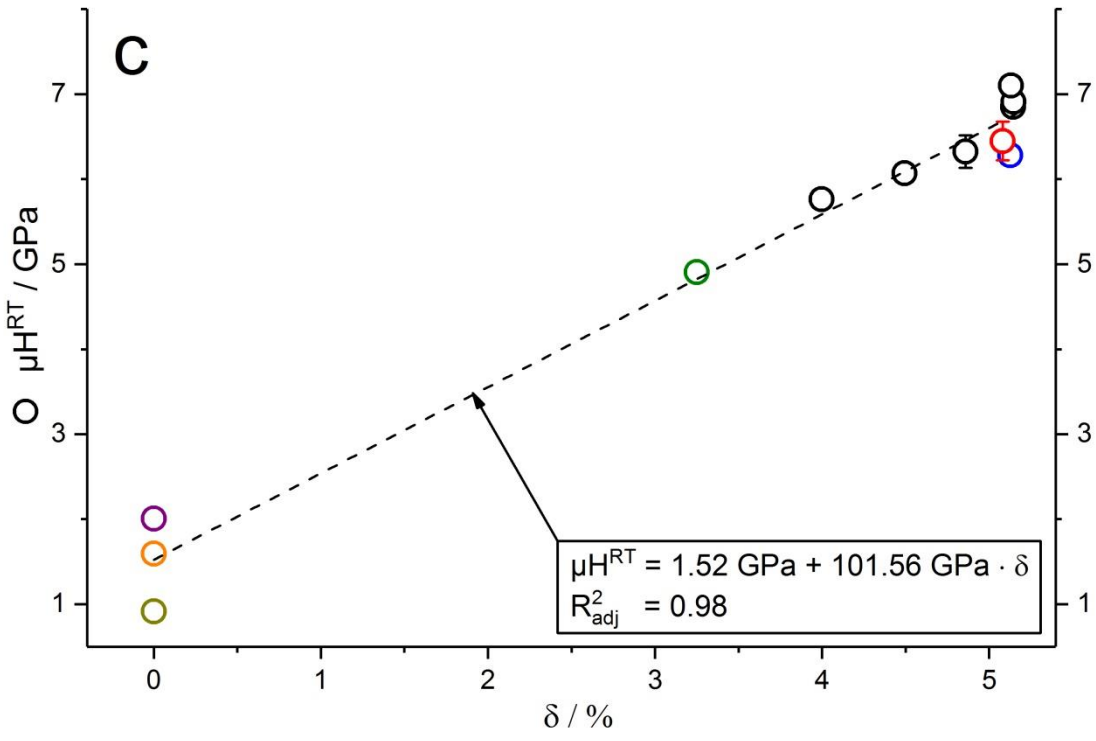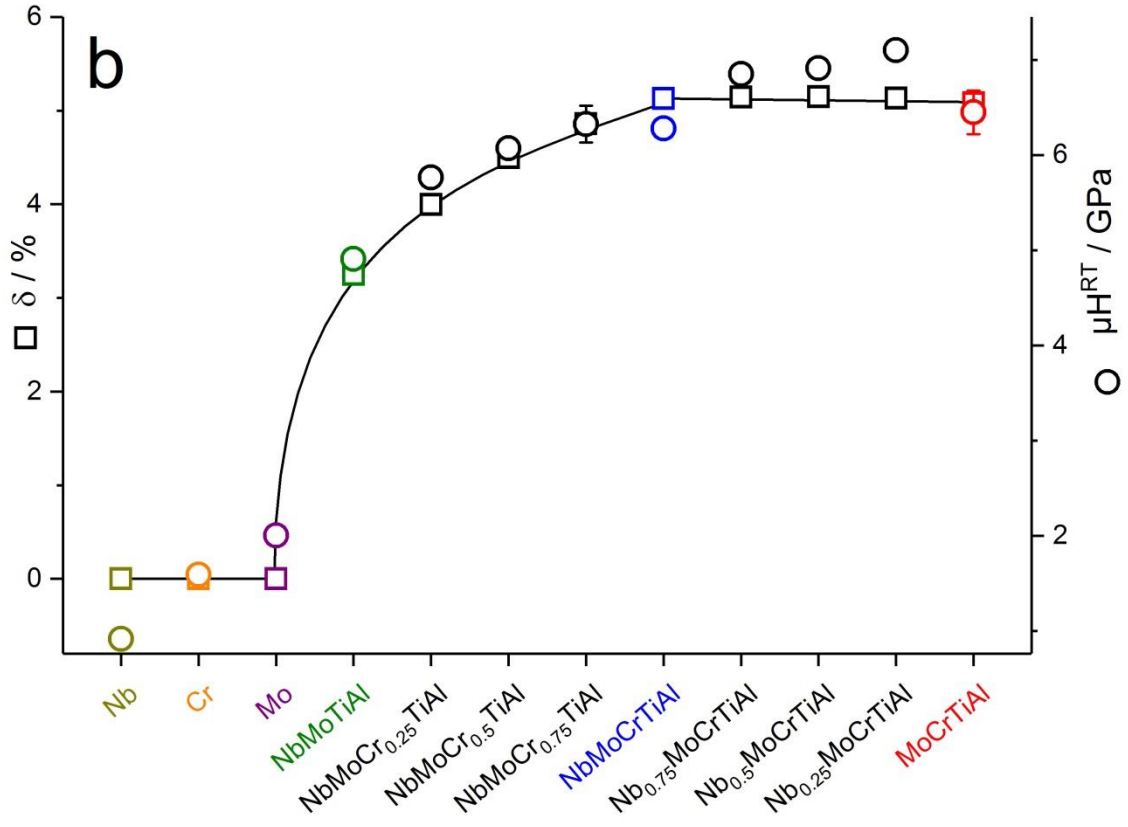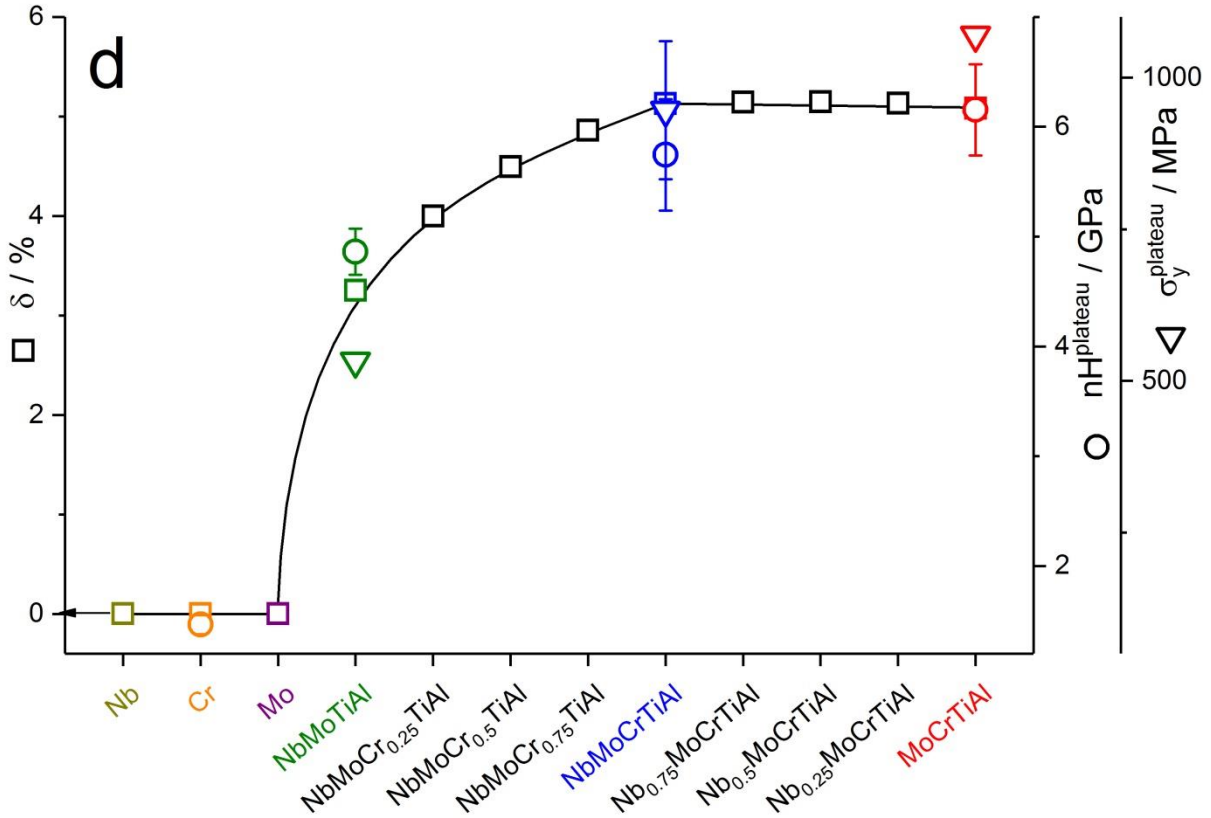
357 over NbMoCrTiAl towards MoCrTiAl, the gradual change of lattice parameter with composition $\frac{1}{a}\frac{\partial a}{\partial x_i}$,

358 serving as a classical measure for the extent of lattice distortion in binary alloys [4], apparently does

359 not reflect the present evolution of microhardness.

360 Fig. 6b visualizes the determined correlation of $\mu H^{RT} = 1.52\,GPa + 101.56\,GPa \cdot \delta$ with $R_{adj}^2 =$

361 0.98 [2]. As pointed out in the previous section, μH^{RT} is altered by a possibly different hardness

362 increase due to thermally activated slip among the alloy series. For this reason, Fig. 6c exemplarily

363 incorporates the plateau values for nanohardness $nH^{plateau}$ as well as yield stress $\sigma_y^{plateau}$ for the

364 quaternary and quinary alloys. Even then, a reasonable correlation of δ and mechanical strength is

365 observed for the present HEA system.

---
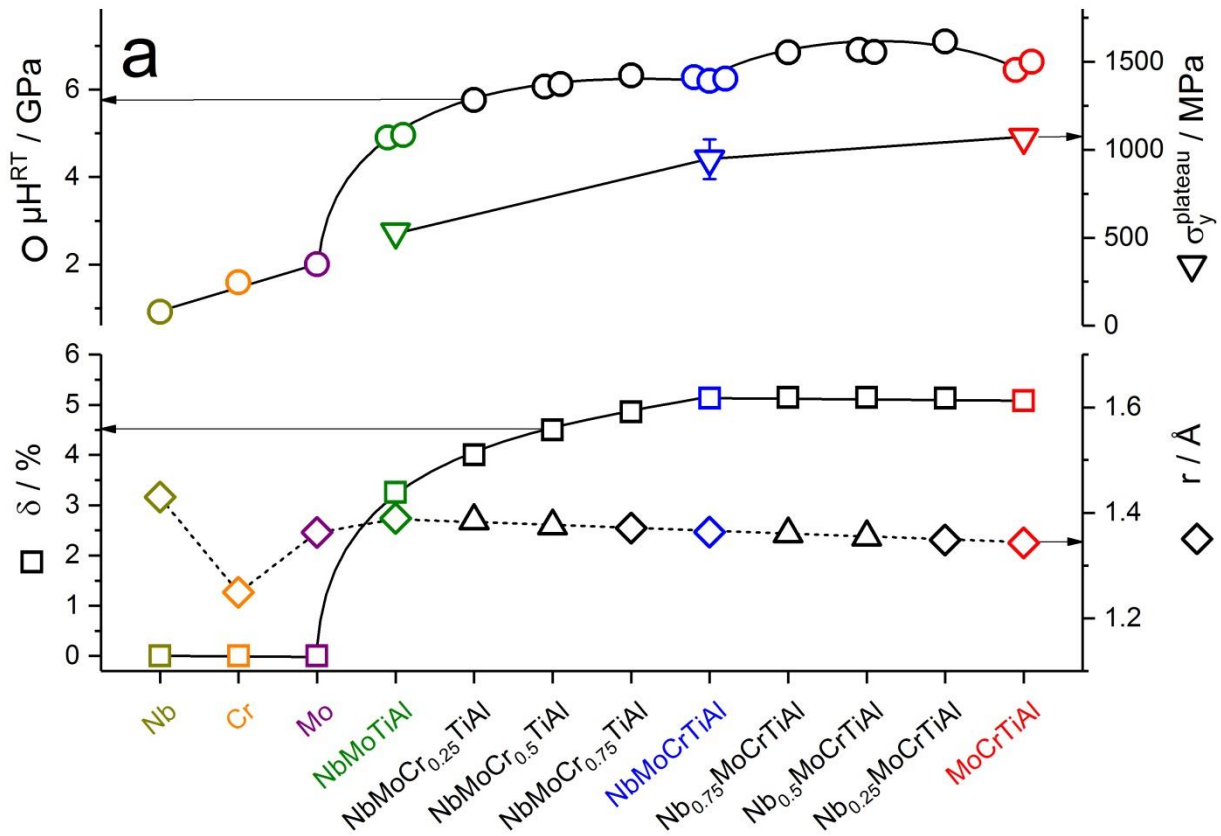
[2] $R_{adj}^2 = 1 - \left(\frac{(1-R^2)\cdot(n-1)}{n-k-1}\right)$ is a modified coefficient of determination R^2 taking the degrees of freedom k and the number data points for data fitting n into account. The coefficient of determination R^2 corresponds to the ratio of the covariance and the product of the standard deviations of the fitted data.

b

c

$\mu H^{RT} = 1.52 \text{ GPa} + 101.56 \text{ GPa} \cdot \delta$

$R_{adj}^2 = 0.98$

Figure 6: a) Assessment of atomic size r and atomic size difference δ using re-calculated radii (lower part of the figure) as well as of microhardness at room temperature μH^{RT} and plateau yield stress $\sigma_y^{plateau}$ (upper part of the figure). Multiple microstructural conditions (higher homogenization temperature, different batches) for various alloys are included here and do not reveal significant variation. b) Correlation of δ / μH^{RT} and according element / alloy composition. c) μH^{RT} evolution with respect to δ reveals linear correlation with $\mu H^{RT} = 1.52 \text{ GPa} + 101.56 \text{ GPa} \cdot \delta$ and $R_{adj}^2 = 0.98$. d) Correlation of δ and $\sigma_y^{plateau}$ as well as $nH^{plateau}$ from Figs. 4b and c, respectively. For all diagrams, error bars which do not exceed the symbol size are omitted. Color coding is consistent for all diagrams.

As already mentioned, the hardness of $Nb_x MoCrTiAl$ alloys with x = 0.25, 0.5 and 0.75 with almost constant atomic size difference apparently exceeds the average hardness of NbMoCrTiAl and MoCrTiAl. In addition to the severely distorted lattice as a major contribution to solid solution strengthening, additional factors might cause the exceeding microhardness of $Nb_{0.25}MoCrTiAl$, $Nb_{0.5}MoCrTiAl$ and especially $Nb_{0.75}MoCrTiAl$.

A change in shear modulus which correlates with the line energy of dislocations could influence dislocation motion. The most obvious deviations from the correlation of μH^{RT} and δ is observed for the alloys with almost constant atomic size difference. Thus, the shear modulus G was determined for

Nb$_x$MoCrTiAl with x = 0, 0.25, 0.5, 0.75, 1 and NbMoTiAl for comparison also in order to cover the entire composition range of the investigated alloys. Shear moduli exhibit only minor changes from about 52 GPa upto about 66 GPa and do not seem to provide a correlation with the observed room temperature microhardness µH^{RT}. Hence, we assume that within the Nb-Mo-Cr-Ti-Al system with varying Cr and Nb concentration, the shear modulus does not play a major role for solid solution strengthening. Although no global superstructure was detected by XRD analyses, different types of ordering might additionally strengthen some of the alloys.

Table 2: Relevant materials properties for the evaluation of composition-depending shear modulus G.

j	nominal composition	annealing condition	porosity	ρ / kg/m^3	v_T / m/s	G / GPa
1	NbMoTiAl	1500 °C, 20 h	0.0078 ± 0.0018	6637 ± 2	2940 ± 15	**57.8 ± 2.2**
5	NbMoCrTiAl	1300 °C, 20 h	0.0116 ± 0.0027	6594 ± 5	3150 ± 18	**66.2 ± 1.0**
6	Nb$_{0.75}$MoCrTiAl	1300 °C, 20 h	0.0127 ± 0.0110	6501 ± 46	2990 ± 2	**58.9 ± 2.5**
7	Nb$_{0.5}$MoCrTiAl	1300 °C, 20 h	0.0083 ± 0.0025	6420 ± 16	3130 ± 1	**63.4 ± 3.4**
8	Nb$_{0.25}$MoCrTiAl	1300 °C, 20 h	0.0080 ± 0.0045	6245 ± 40	2880 ± 1	**52.2 ± 1.0**
9	MoCrTiAl	1200 °C, 20 h	0.014 ± 0.0070	6165 ± 57	2927 ± 29	**53.6 ± 0.5**

4. Conclusions

Providing almost single phase microstructure, dislocation mediated plasticity with ⟨111⟩ Burgers vectors and varying atomic size differences between 3.25 and 5.15 %, NbMoCrTiAl and its derivatives are very well suited for investigating the impact of lattice distortion on the solid solution strengthening in concentrated bcc alloys. In the present article, a correlation between the atomic size difference δ and room temperature microhardness µH^{RT}, namely µH$^{RT} = 1.52$ GPa $+ 101.56$ GPa $\cdot \delta$, was found for a series of alloys Nb-Mo-Cr-Ti-Al including two quaternary and one quinary, equimolar composition. The following conclusions can be drawn:

1. Bcc solid solutions were stabilized by appropriate heat treatments in all investigated alloys and competing phases were accordingly suppressed when gradually reducing the concentration of Nb and Cr.

2. Individual atomic radii of the alloying elements were determined by evaluation of experimentally observed mean atomic radii of all investigated alloys.

3. Although μH^{RT} reasonably correlates with the atomic size difference δ, the magnitude of μH^{RT} is altered by the well-known feature of thermally activated dislocation slip in bcc metals and solid solutions. Thus, combined temperature-dependent mechanical characterization by both nanoindentation and compression tests was utilized to exemplarily assess the athermal strength of the equimolar alloys. Both, $\sigma_y^{plateau}$ as well as $nH^{plateau}$ further support the correlation with δ found for μH^{RT}.

4. Variation of shear moduli remains small within the composition range of the investigated alloys and cannot account for the observed dependence of the hardness of the alloys.

Acknowledgements

References

1   J.-W. Yeh, S.-K. Chen, S.-J. Lin, J.-Y. Gan, T.-S. Chin, T.-T. Shun, C.-H. Tsau, and S.-Y. Chang: Adv. Eng. Mater., 2004, vol. 6, pp. 299–303.

2   D.B. Miracle, and O.N. Senkov: Acta Materialia, 2017, vol. 122, pp. 448-511.

3   C. Varvenne, G.P.M. Leyson, M. Ghazisaeidi, and W.A. Curtin: Acta Materialia, 2017, vol. 124, pp. 660-683

4   R.L. Fleischer: Acta Metallurgica, 1961, vol. 9, pp. 996–1000.

5   R.L. Fleischer: Acta Metallurgica, 1963, vol. 11, pp. 203–209.

6   R. Labusch: physica status solidi (b), 1970, vol. 41, pp. 659–669.

7   I. Toda-Caraballo: Scripta Materialia, 2017, vol. 127, pp. 113–7.

8   I. Toda-Caraballo and P.E.J. Rivera-Díaz-del-Castillo: Acta Materialia, 2015, vol. 85, pp. 14–23.

432   9   N.L. Okamoto, K. Yuge, K. Tanaka, H. Inui, and E.P. George: AIP Advances, 2016, vol. 6, p.
433   125008.

434   10   C. Varvenne, A. Luque, and W.A. Curtin: Acta Materialia, 2016, vol. 118, pp. 164–76.

435   11   Z. Wu, H. Bei, G.M. Pharr, and E.P. George: Acta Materialia, 2014, vol. 81, pp. 428–41.

436   12   S.I. Rao, C. Varvenne, C. Woodward, T.A. Parthasarathy, D. Miracle, O.N. Senkov, and W.A.
437   Curtin: Acta Materialia, 2017, vol. 125, pp. 311–20.

438   13   A. Fernandez-Caballero, J.S. Wrobel, P.M. Mummery, and D. Nguyen-Manh: arXiv preprint
439   arXiv:1705.01844.

440   14   H. Chen, A. Kauffmann, B. Gorr, D. Schliephake, C. Seemüller, J.N. Wagner, H.-J. Christ, and M.
441   Heilmaier: Journal of Alloys and Compounds, 2016, vol. 661, pp. 206–15.

442   15   B. Gorr, F. Mueller, H.-J. Christ, T. Mueller, H. Chen, A. Kauffmann, and M. Heilmaier: Journal
443   of Alloys and Compounds, 2016, vol. 688, Part B, pp. 468–77.

444   16   B. Gorr, F. Müller, M. Azim, H.-J. Christ, T. Müller, H. Chen, A. Kauffmann, and M. Heilmaier:
445   Oxidation of Metals, 2017, pp. 1–11.

446   17   B. Gorr, M. Azim, H.-J. Christ, T. Mueller, D. Schliephake, and M. Heilmaier: Journal of Alloys
447   and Compounds, 2015, vol. 624, pp. 270–8.

448   18   B. Gorr, M. Azim, H.-J. Christ, H. Chen, D.V. Szabo, A. Kauffmann, and M. Heilmaier:
449   Metallurgical and Materials Transactions A, 2016, vol. 47, pp. 961–70.

450   19   J.B. Nelson and D.P. Riley: Proceedings of the Physical Society, 1945, vol. 57, p. 160.

451   20   M.J. Mayo and W.D. Nix: Acta Metallurgica, 1988, vol. 36, pp. 2183–92.

452   21   I.-C. Choi, C. Brandl, and R. Schwaiger: submitted to Acta Materialia.

453   22   K.L. Johnson: Contact Mechanics, Cambridge University Press, 1987.

454   23   K. Lichtenberg, E. Orsolani-Uhlig, R. Rössler and K. A. Weidenmann: Journal of Composite
455   Materials, 2017, 0021998317699867.

456   24   O.N. Senkov, J.M. Scott, S.V. Senkova, D.B. Miracle, and C.F. Woodward: Journal of Alloys and
457   Compounds, 2011, vol. 509, pp. 6043–8.

458   25   G. Chiarotti: in Structure, G. Chiarotti, ed., vol. 24a, Springer-Verlag, Berlin/Heidelberg, 1993,
459   pp. 21–6.

460   26   N. Zárubová: Scripta Metallurgica, 1977, vol. 11, pp. 441–4.

461   27   N. Zárubová and B. Šesták: physica status solidi (a), 1975, vol. 30, pp. 365–74.

462   28   A. Seeger: Zeitschrift für Metallkunde, 2002, vol. 93, pp. 760–77.

463   29 V. Maier, A. Hohenwarter, R. Pippan, and D. Kiener: Scripta Materialia, 2015, vol. 106, pp. 42–5.

464   30   B. Šesták and A. Seeger: Zeitschrift für Metallkunde, 1978, vol. 69, pp. 195–202.

Captions

466   Table 1: Composition in at.% of solid solutions in annealed condition determined by standard-related

467   EDX as well as lattice parameters of the bcc structure; O contents were exemplarily analyzed for

468   NbMoTiAl, NbMoCrTiAl and MoCrTiAl: 780 at.ppm, 312 at.ppm and 289 at.ppm, respectively. N

469   content was below the detection limit for all tested alloys. ♦ highlights EDX on a different batch [14],

470   * were used for re-calculation of the atomic radii.

471   Table 2: Relevant materials properties for the evaluation of composition-depending shear modulus G.

472   Figure 1: Microstructure of alloys with equiatomic composition in homogenized condition, obtained

473   by SEM using BSE contrast imaging (same magnification for all images): (a) NbMoTiAl annealed at

474   1500 °C, (b) NbMoCrTiAl annealed at 1300 °C and (c) MoCrTiAl annealed at 1200 °C, each for 20 h.

475   Certain porosity (black features within the grains) is typical for cast material (< 2 vol.% in all

476   presented alloys) and was randomly distributed in both as-cast (not presented in this article) and

477   as-homogenized state.

478   Figure 2: XRD patterns with logarithmic intensity scale of alloys with equiatomic composition in

479   homogenized condition: (a) NbMoTiAl annealed at 1500 °C, (b) NbMoCrTiAl annealed at 1300 °C

480   and (c) MoCrTiAl annealed at 1200 °C, each for 20 h. Peaks arising from residual Cu-Kβ radiation are

481   indicated by open triangles ▽.

482   Figure 3: Comparison of experimental and re-calculated atomic radii in the elements r_i as well as

483   investigated alloys $\bar{r}_j$. Literature data for Al, Ti (using CN = 12, respectively), Nb, Mo and Cr (using

484   CN = 8), respectively, represented by solid bars are all taken from [25], "Ti*" designates an

485   extrapolation of the atomic radius of bcc Ti corrected by thermal expansion down to room temperature

486   (CN = 8) according to Ref. [24].

487   Figure 4: a) Scheme of the temperature-dependent yield stress of bcc metals and alloys. Experimental

488   results for the temperature dependence of the equiatomic alloys MoCrTiAl, NbMoTiAl and

489   NbMoCrTiAl: b) Microhardness μH^{RT} was obtained at room temperature. Multiple data points

490   represent μH^{RT} obtained for varying homogenization parameters and on different batches (please see

491   Tab. 1). Nanohardness nH was determined between room temperature and 400 °C in order to obtain

492   the plateau nanohardness $nH^{plateau} = nH(400°C)$. c) Compression tests were performed at a

493   consistent strain rate of $10^{-3}s^{-1}$ between 400 °C and 1200 °C depending on the macroscopic ductility

494   of the polycrystalline material in order to obtain the plateau yield stress $\sigma_y^{plateau}$ equal to $\sigma_y^{600°C}$

495   (NbMoCrTiAl, NbMoTiAl) and $\sigma_y^{400°C}$ (MoCrTiAl). The connecting lines are guiding the eyes. Error

496   bars that do not exceed the symbol size are omitted.

497   Figure 5: Secondary electron (SE) contrast image of a Vickers indent (lower right corner) in

498   NbMoCr$_{0.5}$TiAl at room temperature, revealing slip traces in various directions in the vicinity of the

499   indent; slip traces are highlighted by black arrows.

500   Figure 6: a) Assessment of atomic size r and atomic size difference δ using re-calculated radii (lower

501   part of the figure) as well as of microhardness at room temperature μH^{RT} and plateau yield stress

502    $\sigma_y^{plateau}$ (upper part of the figure). Multiple microstructural conditions (higher homogenization

503   temperature, different batches) for various alloys are included here and do not reveal significant

504   variation. b) Correlation of δ / μH^{RT} and according element / alloy composition. c) μH^{RT} evolution

505   with respect to δ reveals linear correlation with $\mu H^{RT} = 1.52$ GPa $+ 101.56$ GPa $\cdot \delta$ and $R_{adj}^2 = 0.98$.

506   d) Correlation of δ and $\sigma_y^{plateau}$ as well as $nH^{plateau}$ from Figs. 4b and c, respectively. For all diagrams,

507   error bars which do not exceed the symbol size are omitted. Color coding is consistent for all diagrams.